Biomass steam-reforming in a low throughput fluidized bed reactor

Farid Aiouache and Kuniyuki Kitagawa
Ecotopia Science Institute, Division of Energy Sciences, Nagoya University,
464-8603 Nagoya, Japan

Abstract

This work presents the results from biomass gasification tests in a low throughput fluidized bed membrane reactor (FBMR) and compares them with two-phase model predictions. The operating temperature was decreased to 550^0C, while an equimolar steam/cellulose ratio was used. The profiles of kinetics limitation and biomass conversion were analysed when a palladium (Pd) membrane for hydrogen separation was used. The produced gases were analysed by gas chromatography, while steam composition and temperature profiles were retrieved by near-infrared imaging (NIRI) technique. As a single membrane tube did not show high permeability rates, the changes in conversions and temperatures profiles were not significant when a Pd membrane was incorporated. The experimental design and procedure allowed us to visualize low radial dispersions in the FBMR.

1- Introduction

The miniaturization of chemical processes is one of the most promising technologies with remarkable growth in the chemical industry. In contrast to the conventional objective in chemical industry, feasibility and applicability of such small equipments have been the prior objective than their productivity and efficiency. The large surface to volume ratio permits multiple design arrangements and analysis under safety conditions. Different types of reactors have been investigated during the last decade with a special concern on those showing several functions. Undoubtedly, hybrid reactors of reaction and separation will occupy the largest domain in chemical reactor design [1, 2]. In this work, we intend to experiment a bubbling fluidized bed reactor (BFBR) with a low throughput and combined with a selective membrane. A dual purpose is aimed beyond this investigation (1) in situ visualization of temperature and vapour distribution during the steam reforming of biomass; (2) comparison between experimental data, the model results and visualization maps in a simplified small size fluidized bed reactor. To our knowledge, this objective has not been experienced yet. A higher homogenisation, low radial dispersions and less carbon deposition are expected.

Assadulah et al. [3, 4, and 5] claimed that $Rh/CeO_2/SiO_2$ was showing a high selectivity with a low carbon deposition for cellulose gasification than the conventional catalysts (dolomite and Nickel supported). In this work, less affordable catalyst is prepared by adding Nickel to Rhodium. The changes of the catalyst activity are investigated by gas chromatography and NIRI technique. We are not aware if this technique has been used previously. However, the spatially resolved infrared imaging (IRI) technique was used by Luss et al. [6] for self-oscillations on supported catalysts and Wolf et al. [7] for monitoring the linear distribution of adsorbed CO coverage on Rhodium supported catalysts. Infrared methods by thermography are still suffering from background interference, accurate emissivity values and detector sensitivities. In this work, near infrared camera is used to map OH band distribution in gas phase and adsorbed on catalyst surface as well. Applying this method may partially circumvent some limiting constraints in the IRI technique : (1) In low throughput BFBR, a negligible NIR beam scattering and high transmittance through the bed are expected due to low

thickness of the optical path; (2) A cheaper window in quarts is used while the IRI requires sapphire or ZnSe materials; (3) Compared with OH band intensities, CO and CO_2 bands show negligible intensities according to HITRAN data bank [8]; (4) For similar detector sensitivity, Accuracy of the temperature obtained by NIR spectroscopy is higher than that from IR spectroscopy [9]. On the other hand, the typical spectrum of NIR spectroscopy of vapour deposition on $Rh/Ni/CeO_2/SiO_2$ catalyst during hydrogen reduction is shown in Figure 1 [10]. The increase of intensity of peaks with time shows OH interaction with catalyst surface, especially ceria due to its weaker reducibility as shown in equation 2. The 1380 nm band is attributed to OH vapour phase while several peaks are overlapped and which are attributed to strong second overtone bands of adsorbed OH with ceria and nickel active sites. Partial shift bands are observed at 1220 due to their interactions with OH of silica matrix. Then, vapor phase map in the BFBR can be obtained by using a NIR camera with a band filter near 1380 nm, while the remaining NIR intensity corresponds to adsorbed OH species. In low throughput reactor, the steam reforming of cellulose will be investigated as follows: (1) In situ OH band visualization; (2) Bimetallic $Rh-Ni/CeO_2/SiO_2$ activity; (3) An example of comparison of experimental data of conversion, product composition and temperature in bubble and emulsion phases, with and without membrane, with those obtained by the two-phase flow model.

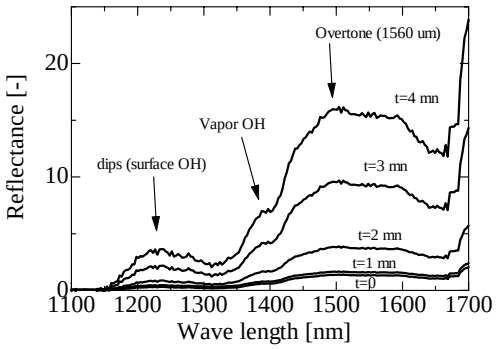

Figure 1 transient spectra during H_2 reduction, Total Pressure $1.013x10^5$ Pa, T=913 K, P_{H2}= $1.013x10^4$ Pa

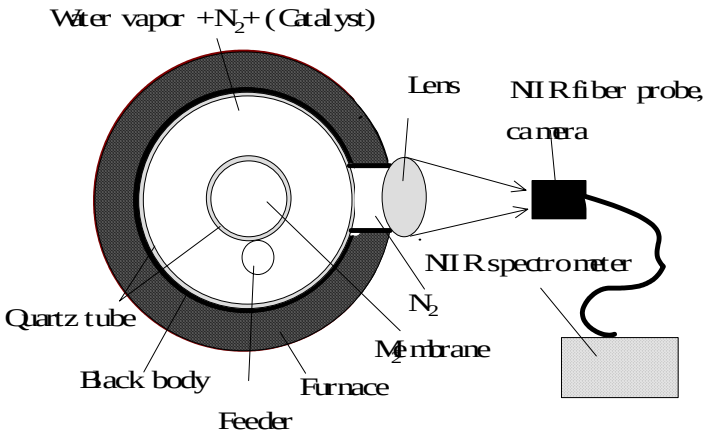

Figure 2 Top view of experimental set-up

2- Experimental section

2-1- Catalyst preparation

The catalyst was prepared according to Assadulah et al. [3] by incipient wetness method. The resulted amounts of Rhodium, CeO_2 and SiO_2 which favoured the higher selectivity onto hydrogen production were selected. Namely, 1.2×10^{-4} mol Rh/g and 0.6 g/g of SiO_2 were added to various amounts of Nickel. The CeO_2/SiO_2 was prepared by the incipient wetness method using the aqueous solution of $Ce((NH_4)_2(NO_3)_6)$ and SiO_2 (Aerosil, 380 m^2/g). After loading CeO_2 and SiO_2, the sample was dried at 383 K for 12 h and then calcinated at 773 K for 3 h under air atmosphere. Rhodium and Nickel were loaded on CeO_2/SiO_2 by impregnation of the support with a solution of $Ni((NO_3)_2.6(H_2O))$ and $Rh(C_5H_7O_2)_3$ in solvent solution. The acetone solvent was then evaporated at room temperature with constant stirring. Then, the catalyst was dried at 383 K for 12 h under nitrogen atmosphere. The final catalyst was pressed, crushed and sieved to 60–150 µm particle size. In each run, 3 g of catalyst was used and pretreated by a hydrogen flow at reaction temperature for 2 hours.

2-2- Apparatus

Figure 2 shows a top view of the experimental set-up. The reactor is made of quarts glass to allow high transparency in near infrared range. The heat required for the endothermic reforming was brought by a side electrical heating. A low continuous throughput of biomass was achieved by changing the micro-feeder vibration speed. The free fall of cellulose was insured by an inner tube inserted from the top. Cellulose was supplied from the top of the reactor together with N_2 flow at 200 cm^3/min (NTP). The reactor was composed of a fluidized bed section at the middle of the reactor. N_2 and steam was supplied from the bottom part. The bottom distributor was made with stainless steel wire gauze of 400 meshes. The distributor was positioned at 0.1 m above the beginning of reactor tube to minimize transient effects at the bed entrance. The product gas was collected and analysed by gas chromatography. Membrane and reactor properties are listed in Table 1. The flowing rate of the effluent gas out of the reactor was measured by a soap membrane meter. The amount of solid carbon (coke on the catalyst and char) was determined by the total amount of gas (mainly CO_2) formed under the air flowing at the reaction temperature.

Table 1 Experimental conditions and reactor properties

Length of reactor tube [m]	0.05
Length of membrane tube [m]	0.01
Inside diameter of the reactor [m]	0.008
Diameter of hydrogen membrane tube [m]	0.004
Thickness of palladium membrane [um]	20
Catalyst particle diameter [mx10^3]	0.06-0.15
Composition of gas products from pyrolysis [-]	
O_2	0.041
CO	0.126
CO_2	0.547
CH_4	0.066
H2	0.218
Flow rates and operating pressures in membrane	
Sweep gas [cm^3/min]	2
Temperature [K]	823-1023
Reaction pressure [kPa]	101.3
Steam to carbon ratio [mol/mol]	1

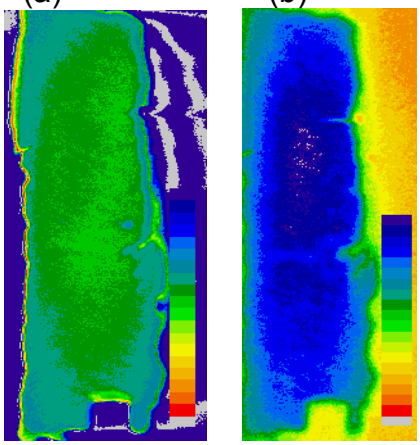

Figure 3. Distribution map of the steam (10 % in N_2) bursting from an inner pipe (a) N_2 flow of 100 cm^3/min STP; (b) N_2 flow 200 cm^3/min).

In order to reach sufficient NIR emissions, the reactor wall was covered with a black velvet ruban to approach black body properties. A rectangular window (10x100 mm2) was kept non-covered for side visualization. NIR camera images with and without an optical filter were recorded at selected temperatures. A Vidicon camera (Hamamatsu 7403) was placed at a distance of 0.45 m from the column. The images (758x512 pixels) were captured by a frame-grabber card (CT3000) and processed (Scion image software).To achieve two and three dimensional views, front and top (60°angle to the cylinder's normal surface) views were selected, respectively.

3- Results

3-1- OH molecules visualization

In order to visualise the catalytic activity of various Nickel added catalysts as cited in section (2-2), OH band of water vapour phase and those adsorbed on catalyst surface were investigated. For gas phase visualization, the reactor set-up was partially modified. A stainless steel tube of 2 mm inner diameter was added from the bottom of the reactor so that two axisymetric co-current flows could be manipulated. Figure 3 shows two image

difference pictures obtained by pixel substraction of their respective two original images acquired with and without steam flow in the inner tube. The vapour phase strikes against the reactor wall for high inner tube flow rates and diffuses to the upper part of the reactor. When the flow rate is small, the vapour flows down from the pipe and accumulates at the bottom of the reactor as the steam is heavier than N_2. It should be noticed that the temperature map (not shown here) issued from pixel values of calibrated NIR camera presented high temperature differences (20-30 K for experimental run at 923 K) with experimental values. For adsorbed OH on catalyst surface, the images were acquired by positioning the camera at 60^0 to the normal of fluidized bed, without disturbing the fluidization and during the transient state of OH adsorption process. The image difference pictures of pure N_2 flow and that of hydrogen flow (10 % STP) through the catalyst bed are shown in Figure 4. It is clearly shown the brightness was caused by the absorption of the incoming NIR radiation by OH bonded molecules on the catalyst surface. During the OH adsorption process, there is a little change in temperature of the catalyst.

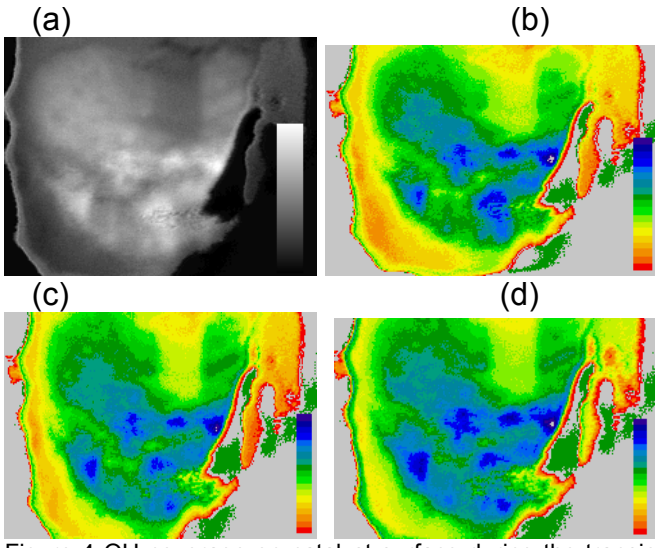

Figure 4 OH coverage on catalyst surface during the transient state (1 minute between image (b), (c) and (d)), (a) is the gray level image of (b), Hydrogen 10 % in N_2, N_2 flow of100 cm^3/min

3-2- Catalyst activity

Figure 5 shows the activity of Rhodium promoted SiO_2-CeO_2 catalyst for cellulose steam reforming. Pure Nickel catalyst exhibited a high reforming activity with high carbon deposition. The conversion of cellulose was 71.5% while the coke-formation rate exceeded 24 mg-coke/g-cat.hr. Furthermore, no coke deposition was detected on pure Rhodium catalyst, but the reforming activity was low (the conversion of cellulose was 56.9%). On the other hand, the detected reforming activity increased slightly on small amounts of Rh promoted Nickel catalysts, while it should be emphasized that the coke-formation rate decreased continuously to zero. It can be concluded that Rhodium and Nickel exhibited synergetic effects in the promoted Rh/CeO2-SiO2 catalyst and possessed higher activity and lower coke deposition. Figure 6 shows the image difference in catalytic activity of pure supported Rhodium and Nickel metals. The half front section of the reactor was occupied by a pure Ni/SiO2/CeO2 and the back side by a pure Rh/SiO2/CeO2. The higher

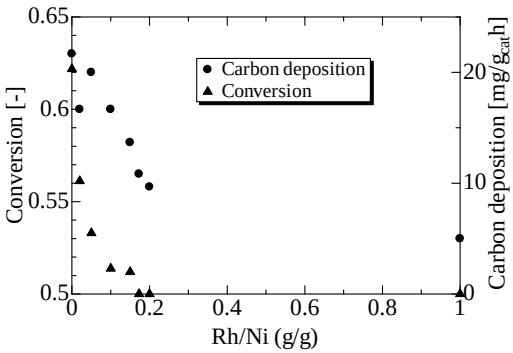

Figure 5 Conversion and carbon deposition profiles at various Rh and Ni ratios, wall temperature of 923 K, F_{H2O}/F carbone=1, N_2 flow of 200 cm^3/min STP

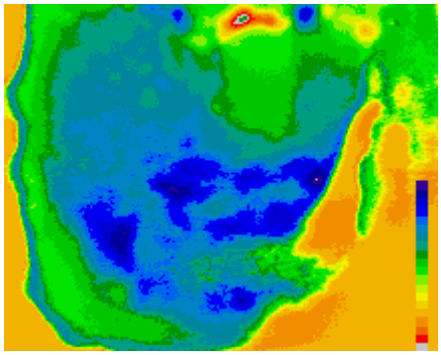

Figure 6 Catalytic activity of pure Ni/ SiO_2/CeO_2 (front side) and pure Rh/SiO_2/CeO_2 (back side), steam 10 % in N_2, N_2 flow of 100 cm^3/min

brightness in Nickel section demonstrates its higher catalytic activity than found in Rhodium.

3-3- Modelling of fluidized bed reactor with palladium membrane

A one dimensional with two-phase model has been developed to predict temperature and concentration gradients along the reactor axis. The effect of reactor bed length on temperatures in bubble and emulsion phases, biomass conversion and product compositions were investigated. Based on dual site formalism of Langmuir-Hinshelwood model, the rate expression of species i is represented by equation (1):

$$r_i = \frac{\sum_{j=1}^{M} \nu_{ij} k_j \left(\prod_{i=1}^{2} (p_i)^{\nu'_{ij}} - \left(1/K_{eqj} \right) \prod_{i=1}^{2} (p_i)^{\nu''_{ij}} \right)}{\left(1 + \sum_{i=1}^{N} K_i p_i \right)^2} \quad (1)$$

While kinetics of carbon reactions (oxidations and reforming) are based on the shrinking-core model [11]

$$r_1 = k_1 p_{O_2 \text{ or } H_2O} m_c^{0.66} \quad (2)$$

Table 2 lists forward kinetic rate constants and equilibrium constants of reactions involved in pyrolysis, reforming and combustion steps. Adsorption constants on Rh-Ni/CeO2-SiO2 catalyst were obtained from Aiouache and kitagawa work [10].

Table 2 Reaction rate constants for cellulose steam reforming

	Pre-exponential factor	Activation energy[J/mol]
k_3[1/s]	41.3	211.1756
k_4 [mol.Pa^{-1}/kg.s]	10.4	77361.77
k_5[mol. Pa$^{0.5}$/kg.s]	7.41x10^{17}	206844.006
k_6[mol Pa$^{0.5}$/kg.s]	4.03	335503.156
k_7[mol/k g .s.Pa]	3.61	62379.942
$K_{eq,4}$ [-]	10.4	-39932.142
$K_{eq,5}$[Pa^2]	65.728	-118931.77
$K_{eq,6}$[Pa^{-1}]	6.32	-78999.628
$K_{eq,7}$[-]	102.3	-153875.512
K_{CH4} [Pa^{-1}]	7.02x10^{-11}	85617.572
K_{H2}[Pa^{-1}]	8.31x10^{-13}	-41836.048
K_{CO}[Pa^{-1}]	9.66x10^{-9}	88577.356
K_{H2O}[Pa^{-1}]	3.98x10^6	80296.612

The model describes the temperature and composition profiles along the vertical direction. The following assumptions were made (1) The FBMR is operating under steady-state conditions; (2) The hydrodynamics are described by the two-phase theory of fluidization with heat and mass exchange between phases; (3) The reaction is mostly carried out in the emulsion phase; (4) Main gas phase and gas-carbon reactions are water gas shift, Boudouard and methanation and methane reforming; (5) Since fine powder catalyst is used, a high radial mixing with negligible mass and heat transfers inside the catalyst is considered; (6) A negligible carbon deposition; (7) No gradient of temperature inside the membrane; (8) No interactions between gas species; (9) No oxidation with hydrogen or palladium membrane; (10) Pyrolysis reaction as instantaneous and the reforming reactions as the limiting step in the global process; (11) The particle scattering and self-emittance are negligible.

The main reactions are shown by equations (3-7).

$2C + 3/2O_2 \longrightarrow CO + CO2$ (3)

$CH4 + H_2O \rightleftharpoons CO + 3H_2$ (4)

$CO + H_2O \rightleftharpoons 3H_2 + CO$ (5)

$CH4 + 2H_2O \rightleftharpoons 4H_2 + CO2$ (6)

$CO_2 + CH4 \rightleftharpoons 2H_2 + 2CO$ (7)

The mass balance along the reactor is expressed by equations (8) and (9)

$$\frac{dF_j^b}{dl} = D_{jb}\frac{\partial^2 C_j^b}{\partial l^2} + k_j^{'} a^b \varepsilon^b A\left(C_j^e - C_j^b\right) + \rho A\sum_{i=1}^{N}\gamma_{ij} r_i^b \qquad (8)$$

$$\frac{dF_j^e}{dl} = D_{je}\frac{\partial^2 C_j^e}{\partial l^2} - k_j^{'} a^b \varepsilon^b A\left(C_j^e - C_j^b\right) + \rho A\sum_{i=1}^{N}\gamma_{ij} r_i^e \qquad (9)$$

$$Q_j = 0.0365\exp\left(-\frac{2465.72}{T}\right)\left(\frac{\pi Dt}{\delta}\right)\left(\sqrt{P_{H_2}^r - P_{H_2}^S}\right)$$

The heat balance in both phases:

$$\frac{\partial T^b}{\partial l} = \frac{1}{Cp^b}\left[\lambda\left(\frac{\partial^2 T^b}{\partial l^2}\right) + \rho\sum_{i=1}^{N}\left(-\Delta Hr^b{}_i\right)\right] \qquad (10)$$

$$\frac{\partial T^e}{\partial l} = \frac{1}{Cp^e}\left[\lambda\left(\frac{\partial^2 T^b}{\partial l^2}\right) + \rho\sum_{i=1}^{N}\left(-\Delta Hr^e{}_i\right)\right] \qquad (11)$$

The bed hydrodynamics are represented as follows

$$\frac{1.75}{\varepsilon_{mf}^3}\mathrm{Re}_{mf}^2 + \frac{150(1-\varepsilon_{mf})}{\varepsilon_{mf}^3}\mathrm{Re}_{mf} - \frac{d_p^3\rho_g(\rho - \rho_g)g}{\mu^2} = 0 \qquad (12)$$

$$d_b = d_{bm} - (d_{bm} - d_{b0})\exp\left(\frac{-0.3l}{Dt}\right), d_{b0} = \frac{1.38}{g^{0.2}}(U_0 - U_{mf})^{0.4}, \qquad (13)$$

$$d_{bm} = 1.64\left[A(U_0 - U_{mf})\right]^{0.4}, u_b = U_0 - U_{mf} + 0.711(gd_b)^{0.5}, \qquad (14)$$

$$\varepsilon_{mf} = \frac{U_0 - U_{mf}}{u_b},\ k_j^{'} = \frac{U_{mf}}{3} + \sqrt{\frac{4D\,\varepsilon_{mf} u_b}{\pi d_b}}, \qquad (15)$$

$$F_j^b = \frac{(U_0 - U_{mf})F_j^0}{U_0}, F_j^e = \frac{U_{mf}F_j^0}{U_0}, \qquad (16)$$

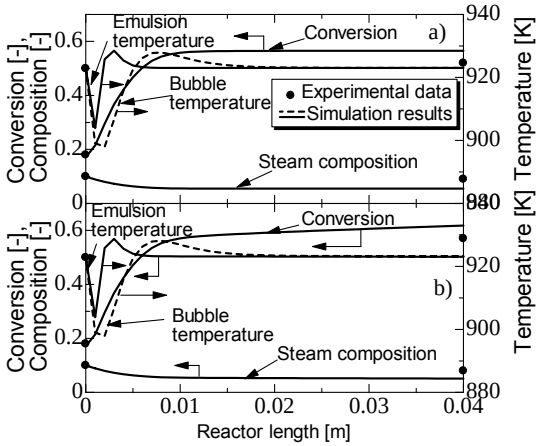

Figure 7 Conversion and temperature profiles in bubble and emulsion phase as a function of bed length. steam (10 % in N_2), N_2 flow of 1 cm^3/min STP., catalyst mass: 3g, wall temperature of 923 K.

4- Discussions

The ordinary differential equations were solved by a Runge-kutta sixth order method with self determination of initial conditions by using EQUATRAN-G (All-purpose equation solver, Omega Simulation Co. Ltd. Japan). Figure 7 compares temperature profiles in bubble and emulsion phases and conversions with and without membrane along the length of the fluidized bed. In both operations, with and without membrane, steep temperature gradients were observed. This hot spot can be observed in Figure 8 which shows the image difference picture between those acquired from fixed and fluidized beds during reaction course. The changes in temperature and, by inference, the reaction conversion were not extended to the all catalytic bed. Due to the low membrane flow rate in the membrane, high values beyond the equilibrium conditions could not be achieved. No further change of the temperature occurred after reactor length of 0.005m for the emulsion phase and 0.017m for the bubble phase as shown in simulation results. In both hot spot cases, temperatures were higher that of the heating elements (923 K). The measured temperature profiles are in line with the subsequent reactions in the global process scheme of cellulose steam reforming, i.e. pyrolysis, partial exothermic oxidation and endothermic steam-reforming of the released products. The similar temperature in both runs, with and without membrane, suggests that any circulation of the solids was not influenced by the membrane. On the other hand, the bubble diameter increased from 0.6

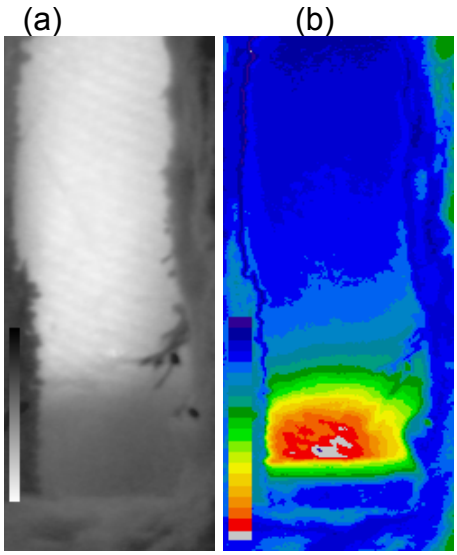

Figure 8 Temperature map in the BFBR, steam (10 % in N_2), N_2 flow of 100 cm^3/min STP. (a) : Original image and (b) Issued from the subtraction of (a) and fixed bed image (not shown), (to red color : higher temperature)

mm at the gas distributor to 7.5 mm at the height of 1.7 cm. Since the distance between reactor wall and membrane tube amounted to 3 mm, slugging was observed in the upper part of the bed. This should lead to a decrease in the separation selectivity compared to the freely bubbling bed since no prefiltering by the mass transfer limitation between bubble and the emulsion phase was present. Due to low permeation rates compared with the total low rates of entering gas, insignificant effect of product separation on syngas yield was detected. The permeation rates in the palladium membrane of hydrogen obtained, for bubble and emulsion phases, was $5x10^{-5}$ mol/m^2.s.Pa and $5.29x10^{-5}$ mol/m^2.s.Pa, respectively, at the distributor level and decreased to $1.21x10^{-5}$ mol/m^2.s.Pa and $6.79x10^{-5}$ mol/m^2.s.Pa, respectively, at reactor length of 0.04 m. Interestingly, the Peclet number which is the ratio between the permeation rate and the feed rate exceeded the value of 19. This value is relatively high to achieve high improvements of hydrogen yield. The molar fractions of CO, water vapor and oxygen decreased exponentially along the reactor axis as shown in Figure 9. Since the rate of the combustion reaction was strongly influenced by intraparticle mass-transport limitations, complete conversion of oxygen was not achieved. The final products, namely carbon dioxide and hydrogen, increased strongly with the contact time until equilibrium limitations. Since the mass-transport limitation affected the combustion of pyrolysis products more strongly than the reforming reactions, the profiles of the desired products CO_2 and H_2 were symmetrical to those of CO and water steam. Furthermore, molar fractions of the intermediate products methane and oxygen were kept in the whole reactor at low level compared with those of hydrogen and carbon dioxide by the reforming steps.

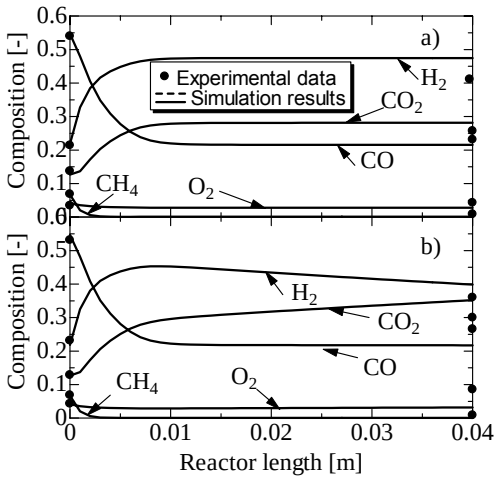

Figure 9 Composition profiles as a function of bed length. steam (10 % in N_2), N_2 flow of 100 cm^3/min STP., catalyst mass of 3g, wall temperature of 923 K.

5- Conclusion

The main observations that were noticed are as follows:

1- Qualitative visualization of OH bands in water vapor phase and on catalyst surface was satisfactory. The quantitative measurements of OH band densities are under development. The preliminary results of temperature profiles in gas phase oscillate between 20K and 30 K at 650 K.
2- The two phase model approached experimental data although several assumptions were considered. In a side study, a sensitivity analysis was carried out by investigating the effect of intraparticle diffusion, diffusion type in membrane and solid particle radiation on conversion, temperature in both phases and product composition.
3- The addition of Nickel to Rhodium supported catalyst improved the catalytic activity with appearance of carbon deposition.
4- This study allowed us to have insight view of the catalyst activity and gas phase vapour profiles during the cellulose steam reforming. Although several non-intrusive techniques are in use for fluidized reactors, they only allow measurements of solid phase properties (porosity, particle and bubble flows). In this work, the results of INRI technique are very encouraging and improvements of experimental set-up are still under investigation.

Nomenclature

A: Cross-sectional occupied by the catalyst bed, m^2

C_i: Concentration of component i in bubble and emulsion phases, respectively, mol/m^3
C_p : specific heat of component i, J/mol.k
d_b: bubble diameter, m
d_{b0}: bubble diameter just above the distributor, m
D_j: effective axial dispersion, m^2/s
D: bed diameter, m
Dt: membrane diameter, m
F_i^b ,F_i^e: molar flow rates of species i in bubble and emulsion phases, respectively
g : acceleration of gravity m/s^2
k_i: forward reaction rate constant, it depends on reaction expression
$K_{eq,j:}$ equilibrium constant, it depends on reaction expression
K_i: adsorption equilibrium constant, Pa^{-1}
l: bed length from the distributor, m
m_c: mass of chars, kg
P_i: partial pressure of species i
Q_j^b:, Q_i^e : permeation rates from the bubble and emulsion phases, respectively, mol/m.s
Re: Reynolds number, dimensionless
r_i: reaction rate, mol/s. kg
T : temperature, K
U_0: superficial velocity, m/s

Greek symbols
v_{ij}: stoickiometric coefficient of component i in reaction j, dimensionless
ρ : density of catalyst bed, dimensionless
ρ_g : density of gas phase, dimensionless
ε : bed porosity, dimensionless
ΔH_r: Reaction enthalpy, J/mol
λ : effective thermal conductivity, J/m.s.K
δ : membrane thickness, μm

Abbreviations
BFBR: nubble fluidized bed reactor
NIRI: near infrared imaging
IRI: infrared imaging
OH: hydroxyl function
mf: minimum fluidization

References

1. Lipnizki, F., R.W. Field and P.K. Ten; J. Membr. Sci., 153, 183–210 (1999)
2. Aiouache, F. and S. Goto; Chem. Eng. Sci. , 58, 2465-2477 (2003)
3. Asadullah, M., Miyazawa, T., Ito, S., Kunimori, K., and K. Tomishige; Appl. Catalysis A: General, 246, 103-116 (2003)
4. Asadullah, M., Miyazawa, T., Ito, S., Kunimori, K., and K. Tomishige; Appl. Catalysis A: General, 255, 169-180 (2003)
5. Asadullah, M., Miyazawa, T., Ito, S., Kunimori, K., and K. Tomishige; Biomass and Bioenergy, 26, 269-279 (2004)
6. Qin, F. and E. E. Wolf; Catalysis letters, 39, 19-25 (1996)
7. Marwaha, M. and D. Luss; AIChE J., 48, 617-624 (2002)
8. S. Clausen; Meas. Sci. Technol., 7, 888-896 (1996)
9. Rothman, L. S., Barbe, A., Chris Benner, D., Brown, L.R., Camy-Peyret, C., Carleer, M. R., Chance, K., Clerbaux, C., Dana, V. and V. M. Devi; J. of Quant. Spect. & Rad. Transf., 82, 5-44 (2003)
10. Aiouache, F. and K. Kitagawa; Catalysis today, under submission
11. Wang, Y. and C.M. Kinoshita; Solar energy, 51,19-25 (1993)